Electronic, optical and thermal properties of the hexagonal and rocksalt-like $Ge_2Sb_2Te_5$ chalcogenide from first-principle calculations

Thierry Tsafack,[1] Enrico Piccinini,[2,a)] Bong-Sub Lee[3,b)] Eric Pop,[4] and Massimo Rudan[2,1]
[1]*DEIS – Dipartimento di Elettronica, Informatica e Sistemistica, University of Bologna, Viale Risorgimento 2, I-40136 Bologna, Italy*
[2]*E. De Castro Advanced Research Center on Electronic Systems ARCES, University of Bologna, Via Toffano 2/2, I-40125 Bologna, Italy*
[3]*Department of Materials Science and Engineering and the Coordinated Science Laboratory, University of Illinois at Urbana-Champaign, Urbana, Illinois 61801, USA*
[4]*Department of Electrical and Computer Engineering, Micro and Nanotechnology Lab, University of Illinois at Urbana-Champaign, Urbana, Illinois 61801, USA*

(Received 4 March 2011; accepted 11 August 2011; published online 26 September 2011)

We present a comprehensive computational study on the properties of rock salt-like and hexagonal chalcogenide $Ge_2Sb_2Te_5$ supported by experimental data. We calculate the electronic structure using density functional theory (DFT); the obtained density of states (DOS) compares favorably with experiments, and is suitable for transport analysis. Optical constants including refractive index and absorption coefficient capture major experimental features, aside from an energy shift owed to an underestimate of the bandgap that is typical of DFT calculations. We also compute the phonon DOS for the hexagonal phase, obtaining a speed of sound and thermal conductivity in good agreement with the experimental lattice contribution. The calculated heat capacity reaches $\sim 1.4 \times 10^6$ J/(m^3 K) at high temperature, in agreement with experiments, and provides insight into the low-temperature range (<150 K), where data are unavailable. © *2011 American Institute of Physics*. [doi:10.1063/1.3639279]

I. INTRODUCTION

Over the past two decades phase-change materials have generated much interest in the area of electronic devices for memory applications thanks to the scaling properties, small energy consumption (<100 fJ/bit),[1] and large number (10^9) of writing cycles.[2] The ability of such materials to switch between the crystalline and the amorphous phase makes them suitable candidates for data storage. In fact, the two phases are associated with large differences in the optical constants and resistivity.[3] Since the late 1960s digital disk-random access memories, phase-change dual disks, re-writable optical media with increasing storage capability and, later on, solid-state non-volatile memories, have been designed and released to the market.

Chalcogenide materials like $Ge_2Sb_2Te_5$ (GST) have extensively been investigated either theoretically or experimentally in order to better understand the nature of their structural, electronic, optical, thermal and electrical properties. X-ray diffraction experiments have provided cell parameters for the hexagonal and the cubic GST (Refs. 4–6), and several hypotheses have also been made about the amorphous phase.[7–9] The GST material is a semiconductor in both the crystalline and the amorphous phase. Its optical bandgap has been estimated around 0.5 eV for the former phase and around 0.7 eV for the latter.[10] Moreover, the optical dielectric constant of the crystalline phase is about twice to three times greater than that of the amorphous phase.[11] The origin of this high optical contrast has been sought in the last years, and it has been linked to resonant bonded *p* states of the crystalline phase that are lost in the amorphous configuration. As a consequence, the remarkable difference in the optical matrix elements associated to the two phases causes the strong optical contrast.[11–13]

In the last decade several models have been proposed[14–16] to describe the snap-back phenomenon in the $I(V)$ characteristic of amorphous GST glasses. In fact, such a feature is fundamental for using the material in the fabrication of solid-state memories. Even though the hexagonal phase is the stable one, the metastable cubic crystals play a major role in device applications. As a matter of fact the amorphous structure of GST stems from a strongly distorted rock salt-like one,[7] and the material can easily switch between the amorphous and the crystalline phase due to Joule heating. The models describing carrier conduction in semiconductors are usually based on the knowledge of the electron and phonon dispersion relations for the material at hand. In a similar manner this type of data are useful for a better understanding of the transport characteristics of the GST material.

This paper describes the results of a comprehensive computational study of the GST chalcogenide, including band structures and optical constants for both the hexagonal and the rock salt-like phases. Two former studies devoted to the hexagonal phase were recently published;[17,18] they are considered here for comparison purposes. Moreover, the vibrational properties of the hexagonal phase are investigated as well, in order to get information on the speed of sound in the material, on the thermal conductivity, and heat

a)Author to whom correspondence should be addressed. Electronic mail: enrico.piccinini@unimore.it.
b)Present address: Tessera Inc., 2025 Orchard Parkway, San Josè, CA, USA.

capacity. The starting point of the analyses is the calculation of the band structure by means of the density-functional (DFT) theory using plane waves as basis set.

After calculating the band structure, the imaginary part $\epsilon_i(\omega)$ of the dielectric tensor $\epsilon_{\alpha\beta}(\omega)$ (including Drude-type contributions) is derived using the Drude-Lorentz expression. The real part $\epsilon_r(\omega)$ is then calculated through the Kramers-Kronig transformation. The Maxwell model allows one to link $\epsilon_r(\omega)$ and $\epsilon_i(\omega)$ to the refractive index $n(\omega)$ and the extinction coefficient $k(\omega)$, as well as the absorption coefficient $\alpha(\omega)$. Two measurable quantities like the optical reflection $R(\omega)$ and transmission $T(\omega)$ are derived from $n(\omega)$ and $k(\omega)$ using exact equations considering multiple reflections in a thin film. They are compared to the corresponding experimental data.

Finally, the phonon density of states (DOS) is calculated through the density-functional perturbation theory (DFPT) for the hexagonal crystalline phase. From this, it is possible to evaluate the sound velocity and the thermal conductivity, which compare well with experimental data on the phonon contribution in hexagonal GST. Moreover, the heat capacity for this phase is obtained over a wide temperature range (5–870 K) by integrating the DOS.

II. METHOD AND CALCULATIONS

The electronic structure has been computed using the DFT equations that are implemented in the Quantum Espresso 4.1 code.[19] This software uses plane waves as a basis set for the expansion of atomic orbitals, and implements periodic boundary conditions. The local density approximation (LDA) by Perdew and Zunger[20] has been considered for the exchange-correlation energy. The electron-ion interactions have been described by means of norm-conserving ionic Bachelet-Hamann-Schluter pseudopotentials without non-linear corrections.[21] The valence configurations are $4s^2 4p^2$, $5s^2 5p^3$, and $5s^2 5p^4$ for Ge, Sb, and Te, respectively. Recent papers[17,22] included explicitly the role of Te $4d$ electrons in the valence configuration (and not as a core contribution). Other authors have pointed out that spin-orbit coupling could play a role for such heavy atoms.[23] As discussed throughout this paper, neglecting these details does not affect the quality of our findings, which favorably compare to experimental evidence.

The cut-off in the kinetic energy was set to 80 Ry, a rather conservative choice since preliminary tests proved that changes in the results become less and less significative roughly beyond 50 Ry.

The first step of the analysis deals with geometry relaxation. As a result of the Born-Oppenheimer approximation, this stage involves the determination of the cell parameters and the atomic coordinates that minimize the energy functional within the adopted numerical approximations.

According to the literature, the stacking sequence of the hexagonal cell is made up of nine layers. Three possible configurations have been proposed, depending on the position of the Sb and the Ge atoms. In an early work Petrov and coworkers[4] proposed the sequence Te – Sb – Te – Ge – Te – Te – Ge – Te – Sb; more recently, Kooi and de Hosson identified a new stacking where all Sb and Ge atoms exchange their positions,[5] while Matsunaga and coworkers suggested that Sb and Te can randomly occupy the same layer, thus resulting in a mixed configuration.[6] Among these configurations, we have adopted that proposed by Kooi and de Hosson, whose total energy is claimed to be the lowest in the computational studies available in the recent literature.[17,18,24] As for the rock salt-like structure, the fact that the phase transition occurs easily from the hexagonal phase suggests that the transformation does not imply a large atomic rearrangement, and the two stackings must share a common background.

The unit cell for the hexagonal phase here considered is then made up of nine atoms and arranged in the stacking sequence Te – Ge – Te – Sb – Te – Te – Sb – Te – Ge, while the rock salt-like structure comes out from shifting the hexagonal Te – Sb – Te – Ge sub-unit along the [210] direction to the next crystallographic plane, thus creating a vacancy site (v) in between. That leads to a unit cell of 27 atoms and three vacancies arranged in the stacking sequence Te – Ge – Te – Sb – Te – v – Te – Sb – Te – Ge repeated three times (Fig. 1). This sequence corresponds to a rock salt-like configuration where Te atoms occupy the Cl sites, while Na positions are filled either by Ge atoms, Sb atoms, or vacancies. The experimental values for the cell parameters are: $a = 4.22$ Å, $c = 17.18$ Å for the hexagonal phase,[25] and $a_0 = 6.02$ Å, corresponding to $a = 4.26$ Å, $c = 52.13$ Å in the equivalent hexagonal system, for the rock salt-like structure.[26] The geometry relaxation resulted in a difference from the experimental data of $\Delta a = 0.08\%$, $\Delta c = -3.02\%$ for the hexagonal phase, and of $\Delta a = -2.05\%$, $\Delta c = -1.8\%$ for the cubic phase. Moreover, a slight shift in the position of internal planes is also found. The calculated shrinkage of the c parameter is consistent with the adopted LDA approximation, and can also be found in the works of Sun *et al.*[24] and of Lee and Jhi,[17] but contrasts with the results of Sosso *et al.*[18]

A $12 \times 12 \times 4$ k-point grid for the hexagonal GST and a $12 \times 12 \times 1$ grid for the rock salt-like phase have respectively been used for the self-consistent calculation in order to

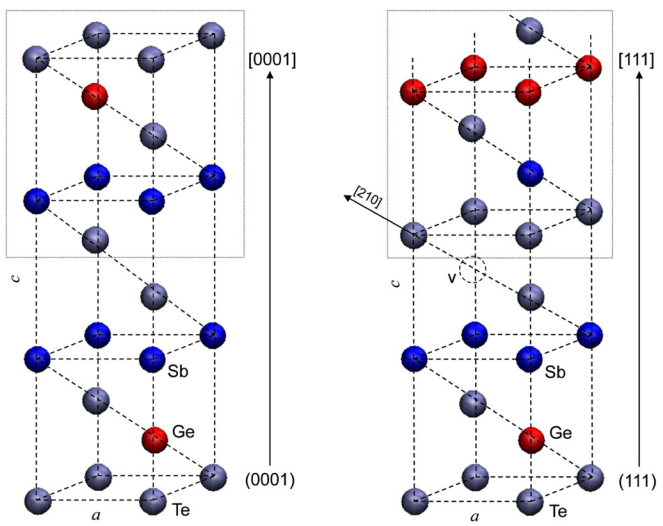

FIG. 1. (Color online) Atomic arrangement of the hexagonal (left) and rock salt-like (right) GST, showing the stacking sequence along the crystalline planes.

determine the ground-state configurations for the two systems at hand. The whole relaxation process for the hexagonal structure took around two days on an 8-processor Linux cluster. Due to the intrinsically higher structural complexity, the computational load for the rock salt cell proved to be four times higher.

As the material optical response is due to transitions within and between valence and conduction bands, the first step toward its calculation, once the ground state is known, involves computing the eigenfunctions and eigenvalues also for the conduction band. A uniform grid of $20 \times 20 \times 20$ was used at this stage for both the hexagonal and the rock salt-like cases. As the optical response strongly depends on the transitions to the conduction band, introducing a dense grid in the calculations increases the accuracy of the calculations themselves. The equations used to build the complex dielectric tensor $\epsilon_{\alpha\beta}(\omega)$ are reported in the appendix.

The last part of the present investigation concerns the vibrational modes. To this aim we have adopted the DFPT approach[27] provided by the Quantum Espresso package. This method sidesteps the need of constructing a superlattice typical of the standard frozen-phonon framework,[28] and allows one to calculate the phonon-dispersion relation. The calculation breaks into three steps, namely, (*i*) computing the ground-state charge density for the unperturbed system, (*ii*) evaluating the phonon frequencies and the dynamical matrices at a given q-vector and, (*iii*) transforming the dynamical matrices back in the real space. The calculation of the ground-state charge density is performed by the self-consistent procedure described earlier. The parameters used in step (*i*) (cutoff energy, convergence threshold, Gaussian smearing, and so on) are the same as those of the band-structure calculation. However, a $4 \times 4 \times 1$-dense k-point grid has been adopted here. The phonon calculation is performed with a $4 \times 4 \times 4$ q-vector grid.

III. RESULTS AND DISCUSSION

A. Band diagram and density of states

In Figs. 2 and 3 we report the electronic band structures along high-symmetry lines around the top of the valence band (VB) and the bottom of the conduction band (CB). The DOS is also shown. The actual calculation was performed in an energy interval larger than that shown, this proving the existence of a few deeper bands. Apart from the extension of the bandgap that will be discussed later, the shape of the bands compares favorably with the calculations of Yamanaka *et al.*[29] and, despite the different parameterization of the pseudopotentials, matches very well the results by Lee and Jhi,[17] both qualitatively and quantitatively. A preliminary band diagram for the rock salt-like phase has recently been published by some of the authors.[30]

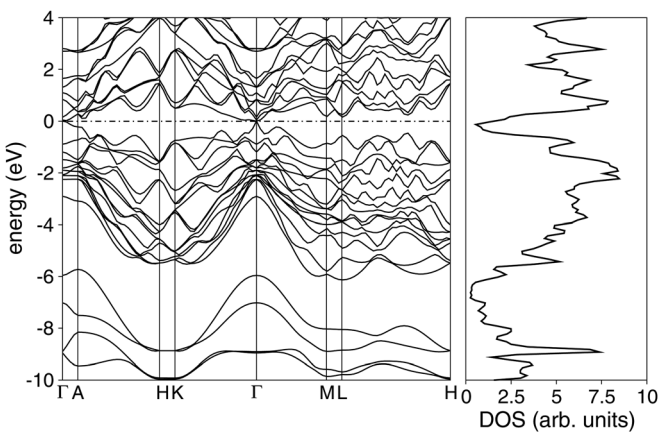

FIG. 2. Band diagram for the hexagonal phase along the high symmetry lines (left), and corresponding density of states (DOS) (right). The predicted Fermi level is located at 0 eV.

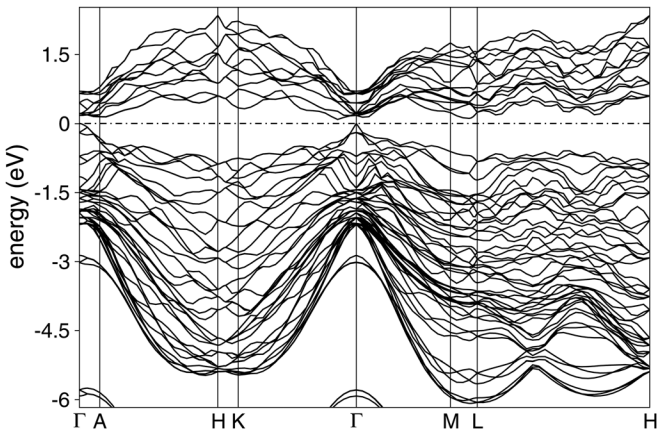

FIG. 3. Band diagram for the rock salt-like phase along the high symmetry lines. The predicted Fermi level is located at 0 eV. Only the valence band and the bottom of the conduction band are shown. An indirect bandgap of ~ 0.1 eV is found along the Γ-K line; the energy gap at Γ is about 0.2 eV. The corresponding DOS is shown in Fig. 4.

As a result of the simulations, a bandgap smaller than what measured in optical experiments (0.5 eV) (Refs. 10 and 11) is found in both cases. More specifically, the hexagonal phase apparently acts as a semi-metal (VB and CB are degenerate at the Γ point), whereas an indirect bandgap of about 0.1 eV is found for the rock salt-like phase. This result is consistent in shape with the findings of optical experiments that indicate an indirect bang gap for this phase.

In the recent works of Lee and Jhi[17] and of Sosso *et al.*[18] a bandgap of about 0.2 eV, smaller than the optically-determined one, is found also for the hexagonal phase. The work of Lee and Jhi and that of Sosso *et al.* do not share the same parameterization of the valence electrons for Te, nor have the same size of the unit cell, but achieve similar results for the bandgap. On the other hand, the shape of the bands found in this work is almost the same as that of Lee and Jhi and, once the conduction band obtained by our calculation is shifted toward higher energies, it can be superimposed almost exactly to that of Lee and Jhi. Moreover, apart from high-frequency oscillations probably related to different interpolating schemes, the calculated DOS for the hexagonal phase is consistent with that of Sosso *et al.* for both the valence and conduction bands. The same situation also holds true for the rock salt-like phase with respect to experimental data (Fig. 4). Furthermore, the reported DOS compares well to that calculated by Zhou and coworkers in a recent work that was published during the revision process of the present paper.[32] One difference between this result and those of

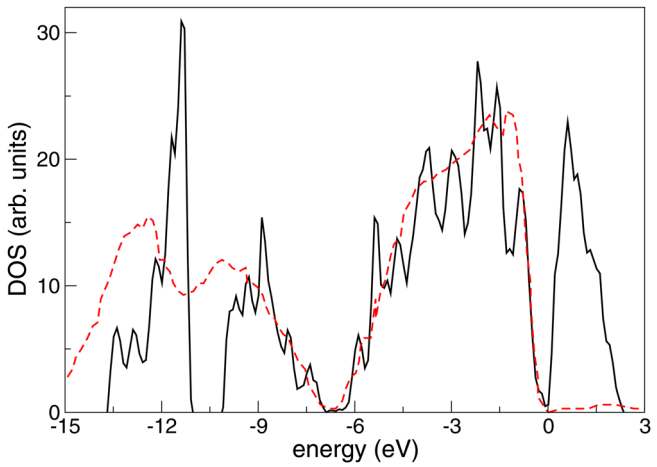

FIG. 4. (Color online) Comparison between calculated (black, continuous line) and experimental[31] (red, dashed line) densities of states for the rock salt-like phase. The non-negligible value for the DOS in the bandgap (around $E = 0$ eV) present in the calculated curve is an artifact due to the smearing of the interpolating Gaussian function.

Sosso *et al.*,[18] of Lee and Jhi[17] and of Zhou *et al.*[32] relies on the approximation of the exchange-correlation potential (LDA instead of the generalized-gradient approximation). The use of different parameterizations for the pseudopotentials and the exchange-correlation term results in different lattice constants and bandgap values.

Nevertheless, the discrepancies in the bandgap among this work and the three references cited above are well within the intrinsic procedure error.[33]

The underestimation of the bandgap is a well-known effect of the DFT calculation and can be corrected by the GW approach and the Bethe-Salpeter equation, to take into account many-body effects.[34] Despite this limitation, DFT is able to reproduce trends, such as a variation in the bandgap due to structural changes. This is the case of the slight increase in the bandgap found in the transition from the hexagonal to the rock salt-like cubic phase. In fact, the stoichiometry of the cubic phase implies that 20% of the lattice positions are represented by vacancies, situated between two well-defined sub-units of the unit cell. Due to the increased distance, the Te-Te bond of the rock salt-like structure is much weaker than that of the hexagonal counterpart. When a melt is quickly undercooled to the amorphous state, the number of weak bonds found in the final structure is quite large, and rings and structural defects are also found.[8,9,35] It has been shown that the formation of vacancies in GST is driven by an increase of the energy gap, this resulting in a lower total energy of the structure.[32] According to the capability of predicting trends of the DFT calculations, since the presence of vacancies and defects grows from the hexagonal to the cubic crystal and from the cubic phase to the amorphous one, a wider bandgap is expected for the latter, consistently with optical determinations. For these reasons, the obtained bands are suitable for being incorporated into a transport simulation scheme that takes into account all of the material phases, including the amorphous one.

The second effect leading to the underestimation of the bandgap is that the measured bandgap depends on the position of the Fermi level. For a *p*-type degenerate semiconductor such as crystalline GST (Ref. 36), the Fermi level is inside the valence band. As a consequence, for an interband optical transition to occur, a photon must be absorbed having an energy larger than the difference between the band edges. Therefore, the optical bandgap of a degenerate semiconductor is larger than the electronic bandgap (Burstein-Moss shift).[37] A proof that the crystalline GST is a *p*-type degenerate semiconductor comes from the experiments based on the Hall effect. Indeed, to explain the temperature-dependence of the Hall coefficient it is necessary to assume that the Fermi level for the hexagonal GST is about 0.1 eV lower than the valence band edge.[10]

B. Optical properties

The calculated real and imaginary parts, $\epsilon_r(\omega)$ and $\epsilon_i(\omega)$, of the dielectric function of the two phases are shown in Fig. 5. They are superimposed with the corresponding experimental relations found in the literature.[10,11,36] To properly compare the experimental and theoretical data it is necessary to remind that the dielectric function depends on the bandgap. The detailed expressions are shown in the appendix. As the DFT calculation underestimates the bandgap, we expect that the calculated dielectric function be rigidly

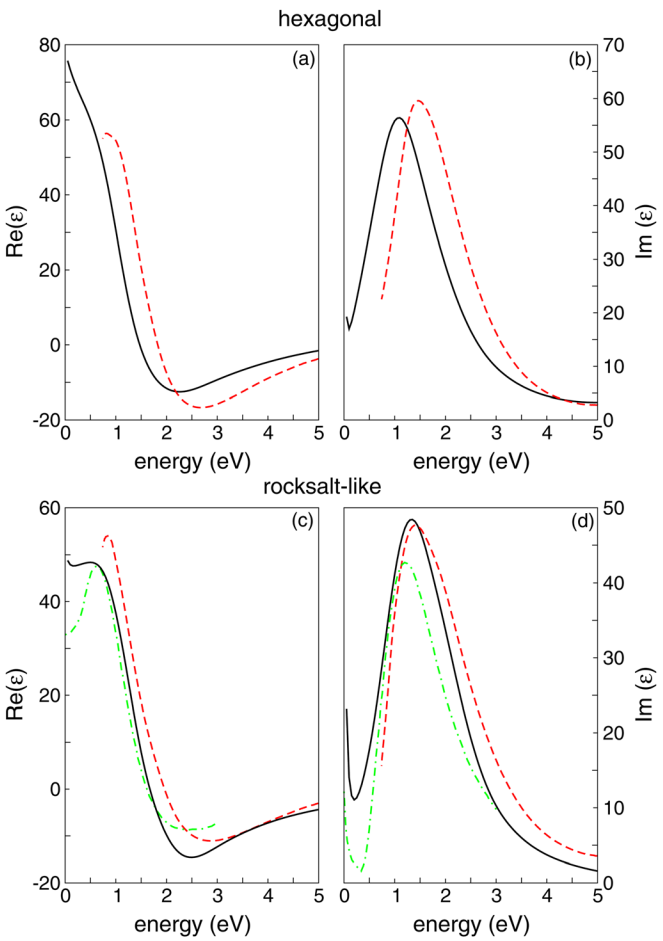

FIG. 5. (Color online) Real part [(a) and (c)] and Imaginary part [(b) and (d)] of the dielectric function for the hexagonal and the rock salt-like phases. The (red) dashed[10,36] and (green) dash-dotted lines[11] show the corresponding functions derived from optical measurements.

shifted on the energy axis toward the lower energies with respect to the experimental one. This indeed happens, and the horizontal offset found between the experimental and theoretical curves (approx. 0.5 eV) complies with such an interpretation. Since DFT does not take into account many-body effects, excitonic effects have been ignored. As typical of chalcogenides, the very large values of the static dielectric constant legitimates this assumption.[12]

The calculated and experimental refractive index $n(\omega)$, along with the extinction and absorption coefficient $k(\omega)$, $\alpha(\omega)$ are also compared (Fig. 6). Similar calculations for the absorption coefficient are available in the literature[17] for the hexagonal phase, though using a different set of pseudopotentials, and are reported in Fig. 6(e) for a straightforward comparison. As $n(\omega)$, $k(\omega)$ and $\alpha(\omega)$ are calculated through $\epsilon_i(\omega)$ and $\epsilon_r(\omega)$, the same reasons accounting for the discrepancies in the dielectric function still hold true. However, we stress a better matching for the rock salt-like data, which may be an evidence of a calculated bandgap closer to the experimental one.

It is also worth noting that the optical determination of the bandgap requires extra calculations. In fact, as shown in the two bottom panels of Fig. 6, the absorption coefficient α can be measured accurately only in a range of energies that is somewhat larger than the optical bandgap. As a consequence, the intercept of the experimental $\alpha(E)$ curve with the energy axis must be found by extrapolation. This is typically done by assuming a power-like relation[38]

$$\alpha h\nu \propto (h\nu - E_g^{\text{opt}})^r, \tag{1}$$

where $h\nu$ denotes the photon energy, E_g^{opt} the optical bandgap, and the exponent r equals 2 for an indirect bandgap. The value of E_g^{opt} is determined by the intersection of $(\alpha h\nu)^{1/r}$ with the energy axis $h\nu$. However, Eq. (1) relies on a model which simplifies the calculated bands. This introduces another error source in the determination of the bandgap, that adds to the ones discussed earlier.

To better compare numerical results with experiments it is also useful to calculate practically measurable quantities such as the optical transmission $T(\omega)$ and reflection $R(\omega)$. As in most cases GST samples are available as thin films on substrates, it is necessary to account for the dependence of $T(\omega)$ and $R(\omega)$ on the film thickness. Four GST samples, two for each phase, having significantly different thicknesses have been prepared and tested. They were sputter-deposited on glass slides and then annealed in an argon atmosphere for 20 mins at 180 °C (for the rock salt-like phase) or 360 °C (for the hexagonal phase). Following the procedure described elsewhere,[11] the optical transmission $T(\omega)$ and reflection $R(\omega)$ were measured at an incidence angle of 0° and 7°, respectively. The optical thickness, estimated by fitting the data to the previously-obtained optical constants, is 15 and 240 nm for the rock salt-like samples, and 12 and 240 nm for the hexagonal samples.

The dependence of $T(\omega)$, $R(\omega)$ on thickness has been evaluated numerically by solving the optical equations[39] for a normally-incident light on a thin layer on top of a thick glass substrate with $n=1.5$ and $k=0$. The results are reported in Fig. 7. In both cases the transmission $T(\omega)$ scales down and, conversely, $R(\omega)$ scales up with thickness, as should be. Interference fringes are present in the spectra near or below the optical bandgap, since multiple reflections occur inside the film and interfere with each other. Once again, the calculated data suffer from the underestimation of the bandgap, but the comparison is quite satisfactory, especially for the thick samples.

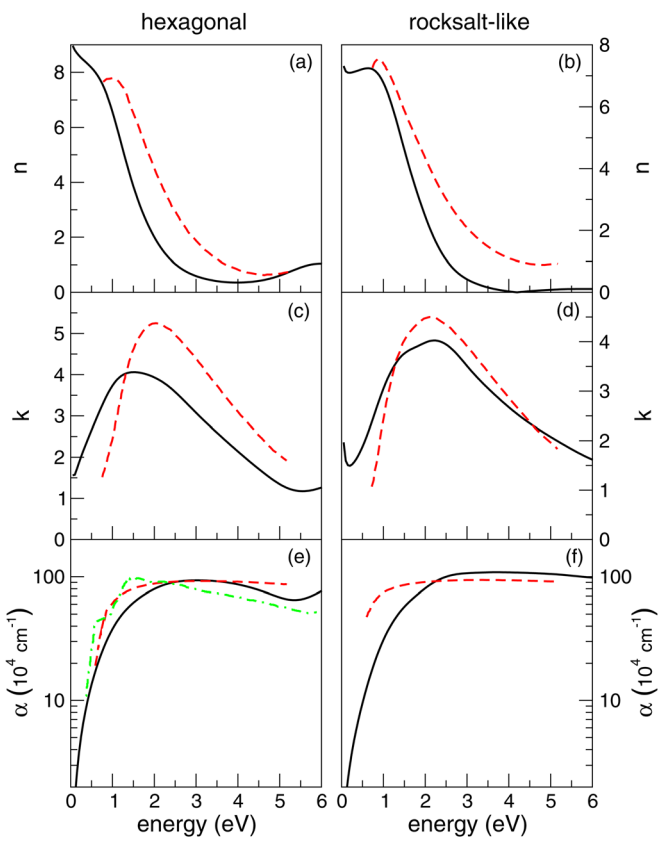

FIG. 6. (Color online) Refractive index [(a) and (b)], extinction coefficient [(c) and (d)], and absorption coefficients [(e) and (f)] for the hexagonal and rock salt-like phases. The (red) dashed line shows experimental data from Ref. 10; the (green) dash-dotted line in panel (e) is taken from Ref. 17. Please note that in the original paper the latter curve has been shifted toward higher energy to correctly reproduce the bandgap.

C. Phonon calculation

The calculation of the full dispersion spectrum is a rather demanding task, and very strict convergence criteria are often required. Therefore, we have limited our analysis to the calculation of the speed of sound and to the DOS with the aim of evaluating the heat capacity of the material, which can be directly compared with experimental data. More details about the complete phonon spectrum are left to future work. The phonon DOS for the hexagonal GST is shown in Fig. 8(a). The general tendency of chalcogenides to have very low phonon frequencies in the range of few tens of meV is confirmed by our findings.[18]

The analogous calculation for the rock salt-like phase resolved into unstable results and a number of imaginary frequencies were also found with any reasonable set of the simulation parameters cited in Sec. II. These findings deserve

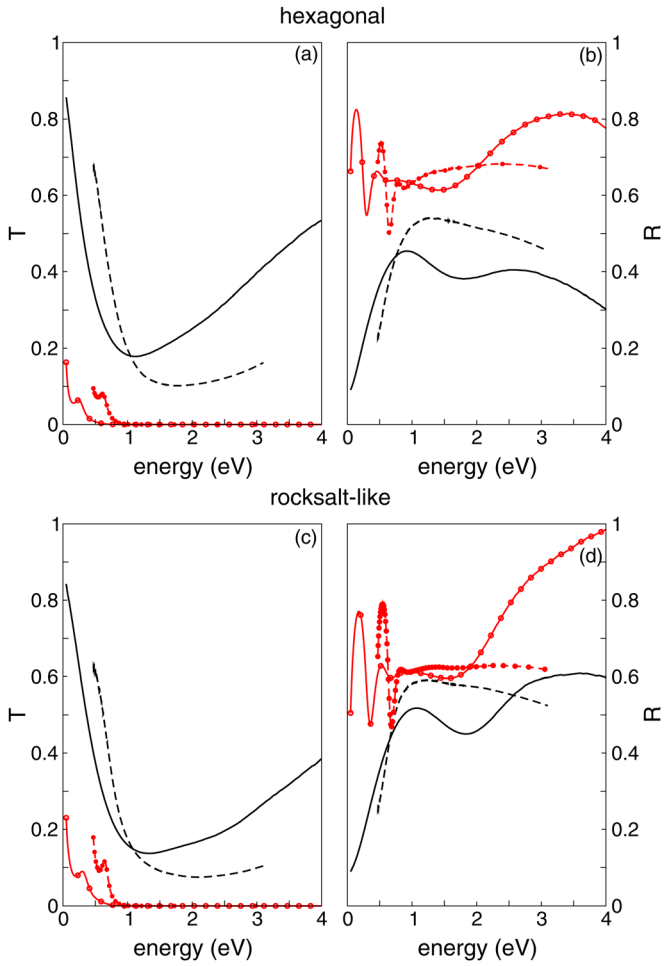

FIG. 7. (Color online) Optical transmission T [(a) and (c)], and reflection R [(b) and (d)] for a thin (12 or 15 nm, black lines) and for a thick sample (240 nm, red lines with solid dots). Calculated values are represented by continuous lines, while dashed lines refers to experiments.

some attention. The presence of imaginary frequencies can in principle be ascribed to a mechanical instability of the simulated structure and/or to convergence issues of the numerical routine. It is well assessed in the literature that the stable crystal for GST is hexagonal, while the rock salt-like structure is metastable, i.e., it corresponds to a relative minimum on the energy scale. As stated in Sec. II, the first stage of this work was devoted to relaxation in order to bring the structure into the lowest energy associated to the imposed atomic arrangement. The relaxed configuration is always a rock salt structure with internal distortions, which become almost insensitive to the convergence conditions when typical threshold values for this kind of simulations are reached. On the contrary, the corresponding simulations for the phonon spectrum presented convergence issues, and even when (apparent) convergence is reached, a significant amount of imaginary frequencies are present. Nevertheless, we are confident on the validity of our results for the electronic and optical properties owing to the consideration above and to the good comparison of our electronic DOS and optical properties to experimental data and other independent simulations, as shown in the previous sections. Convergence problems encountered with the rock salt-like structure appear in fact more correlated to shortcomings of the numerical procedure (probably due to the complexity of the structure itself) than to a real mechanical instability of the simulated crystal. Due to these convergence issues the calculation of the phonon DOS for the rock salt-like phase is omitted from the present publication.

For the hexagonal structure, the calculated speed of sound along the three orthogonal directions is approximately $v_{t1} = 1.74$ nm/ps, $v_{t2} = 2.24$ nm/ps and $v_l = 3.36$ nm/ps for the two transverse and the longitudinal branch, respectively. The last value compares well with the experimentally estimated ~ 3.3 nm/ps reported in the literature.[40] In the high temperature limit, the speed of sound can be exploited to determine the lattice contribution to the minimum thermal conductivity $\Lambda_{\min}$ of the material:

$$\Lambda_{\min} = \frac{1}{2}\left(\frac{\pi}{6}\right)^{1/3} k_B n^{2/3}(v_l + v_{t1} + v_{t2}), \tag{2}$$

where $n \sim 3.4 \times 10^{22}\text{cm}^{-3}$ is the atomic density, and k_B is the Boltzmann constant. The lattice contribution to the minimum thermal conductivity is $\Lambda_{\min} = 0.43$ W/(m K), a lower value than those observed in experiments for the hexagonal phase, which also include an electronic contribution.

However, this result must be interpreted with care, and three aspects deserve attention. First, it should be pointed out that the hexagonal phase is the only stable phase existing at high temperatures (typically above 600 K), and data often refer to that range. Next, according to Reifenberg and coworkers,[41] the GST thermal conductivity depends also on the film thickness. For the hexagonal phase they found a decrease from 1.76 W/(m K) for a 350-nm thick sample to 0.83 W/(m K) for a 60-nm thick sample. Finally, the carrier density in hexagonal crystalline GST is relatively large and electrical carriers also contribute to the heat transport. Experiments have estimated that the electrical contribution is roughly equivalent to the lattice contribution,[42] thus leading to an overall conductivity about twice that of $\Lambda_{\min}$ calculated above. Thus, taking into account these remarks, $\Lambda_{\min}$ is consistent with the phonon contribution in the experiments.

A further confirmation about the validity of the reported DOS comes from a comparison of the calculated heat capacity of GST with that experimentally-determined by Kuwahara and co-workers.[43] Let $E = \hbar\omega$ be the energy of the phonon; the heat capacity can be calculated from the simulated phonon DOS by means of:

$$C = \int_0^\infty E \frac{\partial f_{BE}(E)}{\partial T} \text{DOS}(E) dE \tag{3}$$

where $f_{BE}(E) = \{\exp[E/(k_B T)] - 1\}^{-1}$ is the Bose-Einstein distribution function, and T is the temperature. The calculated and experimental data are reported in Fig. 8 up to 870 K, which corresponds to the approximate melting temperature of GST. According to Kuwahara, the experimental heat capacity slightly increases in the high-temperature region, as the result of structural relaxation of point defects. However, the integral in Eq. (3) includes only the lattice contribution to heat capacity, and thus predicts a saturating value in the classical limit at high temperature. Nevertheless, the

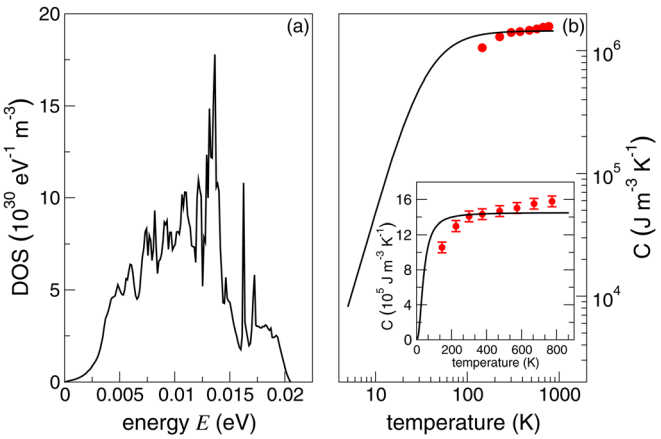

FIG. 8. (Color online) (a) Phonon density of states for the hexagonal phase. (b) Heat capacity for hexagonal GST calculated using data from the panel (a) and Eq. (3) (black line) compared to experimental data (solid red dots) taken from Ref. 43. The inset shows the same data in the linear scale to better represent the region above room temperature, and the error bars for the experimental data.

comparison is good, and calculated data are consistent with experiments in the whole range examined. In addition, these calculations provide an estimate of the heat capacity of hexagonal GST in the temperature range where experimental data are unavailable ($T < 150$ K).

IV. CONCLUSION

In this paper, we reported the electronic and optical properties for the hexagonal and rock salt-like phases of the $Ge_2Sb_2Te_5$ chalcogenide.

The electronic band diagram and DOS were calculated using the density functional theory combined with planes waves, norm-conserving pseudo-potentials and the local density approximation implemented in the code Quantum Espresso. The band diagram and DOS for the hexagonal phase are in good agreement with those reported in the literature. Even though DFT equations are known to underestimate the bandgap, the shape of the bands confirms the existence of an indirect bandgap for the rock salt-like cubic phase, and the DOS of the latter correctly compares to previously published data. The calculation also showed a tendency of the bandgap to increase with respect of the degree of disorder of the cell. This result makes the band diagrams suitable to be used in transport simulations that describe the electrical behavior of GST.

The dielectric function was obtained implementing the Drude-Lorentz expression and the Kramers-Kronig relationships. Furthermore, the refractive index, the extinction and absorption coefficients were derived from the Maxwell model. By incorporating these functions into equations including multiple internal reflection, the optical transmission and reflection for a thin chalcogenide film deposited on a glass substrate were calculated and then compared to experiments. Most of the differences in the comparison can be ascribed to the underestimation of the bandgap.

Moreover, the density functional perturbation theory allowed us to calculate also the phonon DOS for the hexagonal phase. The analysis of the acoustic modes for the hexagonal phase led to reasonable values for both the speed of sound and the minimum thermal conductivity at room temperature. The heat capacity from 5 K up to the melting temperature is also presented, in good agreement with experimental data at high temperature, and providing insight into the low temperature range ($T < 150$ K) where data are unavailable.

ACKNOWLEDGMENTS

The authors appreciate the helpful ideas and suggestions from Professor C. Jacoboni and Professor R. Brunetti (University of Modena and Reggio Emilia), Professor P. Giannozzi (University of Udine), and Dr. S. Pamidighantam (National Center of Supercomputing Applications at the University of Illinois). The authors also want to credit Dr. A. Calzolari and Dr. A. Ferretti (University of Modena and Reggio Emilia) for their support in the start-up of the simulation environment. Special thanks are also due to Professor J.R. Abelson and Professor S.G. Bishop for useful discussions and support. B.-S. Lee was supported by the National Science Foundation under Awards No. DMR 07-06267. The experimental samples were supplied by Dr. Byung-ki Cheong at Korea Institute of Science and Technology, and the optical properties were measured in the Frederick Seitz Materials Research Laboratory Central Facilities, University of Illinois, which are partially supported by the U.S. Department of Energy under Grants DE-FG02-07ER46453 and DE-FG02-07ER46471. E. Pop acknowledges support from the Materials Structures and Devices (MSD) Focus Center, under the Focus Center Research Program (FCRP), a Semiconductor Research Corporation entity, and the Office of Naval Research (ONR) Young Investigator Program (YIP) Grant No. N00014-10-1-0853. Part of this work has been carried on under the Grant No. 34524/2007 of the Intel Corporation, whose support is gratefully acknowledged.

APPENDIX: DERIVATION OF THE OPTICAL PROPERTIES FROM THE BAND DIAGRAM

In the framework of band theory without electron-hole interaction, the dielectric tensor $\epsilon_{\alpha\beta}$ is defined as

$$\epsilon_{\alpha\beta}(\omega) = 1 + \frac{e^2}{\varepsilon_0 \Omega m^2} \sum_{n,n'} \sum_{\mathbf{k}} \frac{M_{\alpha\beta}^{nn'} [f(E_{\mathbf{k}n}) - f(E_{\mathbf{k}n'})]}{(E_{\mathbf{k}n'} - E_{\mathbf{k}n})^2} + \left[\frac{1}{(\omega_{\mathbf{k}n'} - \omega_{\mathbf{k}n}) + \omega + i\Gamma\omega} + \frac{1}{(\omega_{\mathbf{k}n'} - \omega_{\mathbf{k}n}) - \omega - i\Gamma\omega} \right] \tag{A1}$$

with $\Gamma \to 0^+$. In Eq. (A1) e, m and Ω are the electron charge and mass, and the volume of the lattice cell, respectively; $E_{\mathbf{k}n}$ are the eigenvalues of the Hamiltonian and $f(E_{\mathbf{k}n})$ is the Fermi distribution function accounting for the band occupation. Letting $\omega_p = \sqrt{(e^2 N)/(\varepsilon_0 m)}$ be the plasma frequency with N standing for the number of electrons per unit volume,

and $\Delta = \left[(\omega_{\mathbf{k}n'} - \omega_{\mathbf{k}n})^2 - \omega^2\right]^2 + \Gamma^2\omega^2$, the imaginary part $\epsilon_{i\alpha\beta}(\omega)$ of the dielectric tensor $\epsilon_{\alpha\beta}(\omega)$ is given by the following Drude-Lorentz expression:

$$\epsilon_{i\alpha\beta}(\omega) = \frac{\omega_p^2}{Nm\Omega}\left[\sum_{n,\mathbf{k}} \frac{df(E_{\mathbf{k}n})}{dE_{\mathbf{k}n}} \frac{\eta\omega M_{\alpha\beta}^{nn}}{\omega^4 + \eta^2\omega^2} + 2\sum_{n,n'}\sum_{\mathbf{k}} \frac{f(E_{\mathbf{k}n})}{E_{\mathbf{k}n'} - E_{\mathbf{k}n}} \frac{\Gamma\omega M_{\alpha\beta}^{nn'}}{\Delta}\right], \tag{A2}$$

where the original sum over n and n' of Eq. (A1) has been split into two terms, the former accounting for valence-to-valence (or conduction-to-conduction) intraband transitions ($n' = n$), the latter standing for transitions from states belonging to the valence band (index n) to states belonging to the conduction band (index n'). In the summands, the squared matrix elements $M_{\alpha\beta}^{nn'}$ are weighted by a smearing coefficient (η or Γ), and by a factor depending on the Fermi distribution function for interband transitions, or on its derivative for the intraband contribution. Considering that the derivative is substantially zero except in the region close to the Fermi level, the dielectric tensor is dominated by interband transitions, as expected. Nevertheless, a few states near the top of the valence band can be empty due to thermal excitations and, conversely, a small amount of states in the conduction band are occupied. As a consequence, a number of intraband transitions occur, that are described by the first summand of Eqs. (A2) and (A3). Accounting for such transitions is useful to better reproduce the experimental behavior.

In order to keep the Drude-Lorentz approximation valid, the two smearing coefficients η and Γ must be small, even though not vanishing. For the case described in the text they were treated as fitting parameters and both set to 1.0 for the hexagonal phase and to 0.8 and 0.3, respectively, for the cubic phase.

The real $\epsilon_{r\alpha\beta}(\omega)$ part of the dielectric tensor is then calculated applying the Kramers-Kronig relationship to Eq. (A2):

$$\epsilon_{r\alpha\beta}(\omega) = 1 - \frac{\omega_p^2}{Nm\Omega}\left[\sum_{n,\mathbf{k}} \frac{df(E_{\mathbf{k}n})}{dE_{\mathbf{k}n}} \frac{\omega^2 M_{\alpha\beta}^{nn}}{\omega^4 + \eta^2\omega^2} - 2\sum_{n,n'}\sum_{\mathbf{k}} \frac{f(E_{\mathbf{k}n})}{E_{\mathbf{k}n'} - E_{\mathbf{k}n}} \frac{(\Delta - \Gamma^2\omega^2) M_{\alpha\beta}^{nn'}}{\Delta}\right]. \tag{A3}$$

The squared matrix elements $M_{\alpha\beta}^{nn'}$ reveals the tensorial nature of $\epsilon_{\alpha\beta}(\omega)$ and are defined as follows:

$$M_{\alpha\beta}^{nn'} = \langle u_{\mathbf{k}n'} | \mathbf{p}_\alpha | u_{\mathbf{k}n} \rangle \langle u_{\mathbf{k}n} | \mathbf{p}_\beta^\dagger | u_{\mathbf{k}n'} \rangle \tag{A4}$$

where $|u_{\mathbf{k}n}\rangle$ is a factor of the single particle Bloch function obtained by the Kohn-Sham DFT calculation, and $\mathbf{p}_\alpha$ is the momentum operator along the α direction.

In a principal system, the off-diagonal elements of the dielectric tensor are zero and, for perfectly isotropic materials, the diagonal elements are equal. For the two systems considered here, only two eigenvalues out of three are equal. In order to compare results with experimental data where isotropy is assumed, the eigenvalues of the dielectric tensor have been averaged to obtain a unique function.

The refractive index $n(\omega)$, the extinction coefficient $k(\omega)$ and the absorption coefficient $\alpha(\omega)$ are calculated by means of the Maxwell model through the following relationships:

$$n(\omega) = \sqrt{\frac{\sqrt{\epsilon_r(\omega)^2 + \epsilon_i(\omega)^2} + \epsilon_r(\omega)}{2}}, \tag{A5}$$

$$k(\omega) = \sqrt{\frac{\sqrt{\epsilon_r(\omega)^2 + \epsilon_i(\omega)^2} - \epsilon_r(\omega)}{2}}, \tag{A6}$$

$$\alpha(\omega) = \frac{\omega}{cn(\omega)}\epsilon_i(\omega) = \frac{2\omega}{c}k(\omega). \tag{A7}$$

where the symbols ϵ_r and ϵ_i without superscripts represent an average function determined as described above.

[1] F. Xiong, A. D. Liao, D. Estrada, and E. Pop, Science **332**, 568 (2011).
[2] H.-S. P. Wong, S. Raoux, S. B. Kim, J. Liang, J. P. Reifenberg, B. Rajendran, M. Asheghi, and K. E. Goodson, Proc. IEEE **98**, 2201 (2010).
[3] S. R. Ovshinsky, Phys. Rev. Lett. **21**, 1450 (1968).
[4] I. I. Petrov, R. M. Imamov, and Z. G. Pinsker, Sov. Phys. Crystallogr. **13**, 339 (1968).
[5] B. J. Kooi and J. T. M. de Hosson, J. Appl. Phys., **92**, 3584 (2002).
[6] T. Matsunaga, N. Yamada, and Y. Kabota, Acta Crystallogr. B **60**, 685 (2004).
[7] A. Kolobov, P. Fons, A. I. Frenkel, A. L. Ankudinov, J. Tominaga, and T. Uruga, Nature Mat. **3**, 703 (2004).
[8] J. Akola and R. O. Jones, Phys. Rev. B **76**, 235201 (2007).
[9] S. Caravati, M. Bernasconi, T. D. Kühne, M. Krack, and M. Parrinello, Appl. Phys. Lett. **91**, 171906 (2006).
[10] B.-S. Lee, J. R. Abelson, S. G. Bishop, D.-H. Kang, B. Cheong, and K.-B. Kim, J. Appl. Phys. **97**, 093509 (2005).
[11] K. Shportko, S. Kremers, M. Woda, D. Lencer, J. Robertson, and M. Wuttig, Nature Mat. **7**, 653 (2008).
[12] W. Welnic, S. Botti, L. Reining, and M. Wuttig, Phys. Rev. Lett. **98**, 236403 (2007).
[13] B. Huang and J. Robertson, Phys. Rev. B **81**, 081204(R), (2010).
[14] A. Pirovano, A. L. Lacaita, A. Benvenuti, F. Pellizzer, and R. Bez, IEEE Trans. Electron Devices **51**, 452 (2004).
[15] D. Ielmini and Y. Zhang, J. Appl. Phys. **102**, 054517 (2007).
[16] F. Buscemi, E. Piccinini, R. Brunetti, M. Rudan, and C. Jacoboni, J. Appl. Phys. **106**, 103706 (2009).
[17] G. Lee and S.-H. Jhi, Phys. Rev. B **77**, 153201 (2008).
[18] G. C. Sosso, S. Caravati, C. Gatti, A. Assoni, and M. Bernasconi, J. Phys.: Condens. Matter **21**, 245401 (2009).
[19] P. Giannozzi, S. Baroni, N. Bonini, M. Calandra, R. Car, C. Cavazzoni, D. Ceresoli, G. L. Chiarotti, M. Cococcioni, I. Dabo, A. Dal Corso, S. de Gironcoli, S. Fabris, G. Fratesi, R. Gebauer, U. Gerstmann, C. Gougoussis, A. Kokalj, M. Lazzeri, L. Martin-Samos, N. Marzari, F. Mauri, R. Mazzarello, S. Paolini, A. Pasquarello, L. Paulatto, C. Sbraccia, S. Scandolo, G. Sclauzero, A. P. Seitsonen, A. Smogunov, P. Umari, and R. M. Wentzcovitch, J. Phys.: Condens. Matter **21**, 395502 (2009).
[20] J. P. Perdew and A. Zunger, Phys. Rev. B **23**, 5048 (1981).
[21] X. Gonze, R. Stumpf, and M. Scheffler, Phys. Rev. B **44**, 8503 (1991).
[22] G.-S. Do, J. Kim, S-H. Jhi, S. G. Louie, and M. L. Cohen, Phys. Rev. B **82**, 054121 (2010).
[23] E. van Lenthe, J. G. Snijders, and E. J. Baerends, J. Chem. Phys. **105**, 6505 (1996).
[24] Z. Sun, J. Zhou, and R. Ahuja, Phys. Rev. Lett. **96**, 055507 (2006).
[25] I. Friedrich, V. Weidenhof, W. Njoroge, P. Franz, and M. Wuttig, J. Appl. Phys. **87**, 4130 (2006).
[26] Y.-J. Park, J.-Y. Lee, M.-S. Youm, Y.-T. Kim, and H.-S. Lee, J. Appl. Phys. **97**, 093506 (2005).

[27]S. Baroni, S. de Gironcoli, A. Dal Corso, and P. Giannozzi, Rev. Mod. Phys. **73**, 515 (2001).
[28]K. Parlinski, Z. Q. Li, and Y. Kawazoe, Phys. Rev. Lett. **78**, 4063 (1997).
[29]S. Yamanaka, S. Ogawa, I. Morimoto, and Y. Ueshima, Jpn. J. Appl. Phys. **37**, 3327 (1998).
[30]E. Piccinini, T. Tsafack, F. Buscemi, R. Brunetti, M. Rudan, C. Jacoboni, Proc. of the 2008 Int. Conf. on Simulation of Semiconductor Processes and Devices (SISPAD), 2008, p. 229.
[31]J. J. Kim, K. Kobayashi, E. Ikenaga, M. Kobata, S. Ueda, T. Matsunaga, K. Kifune, R. Kojima, and N. Yamada, Phys. Rev. B **76**, 115124 (2007).
[32]J. Zhou, Z. Sun, Y. Pang, Z. Song, and R. Ahuja, Eur. Phys. Lett. **95**, 27002 (2011).
[33]F. Gygi and A. Baldareschi, Phys. Rev. Lett. **62**, 2160 (1989).
[34]G. Onida, L. Reining, and A. Rubio, Rev. Mod. Phys. **74**, 601 (2002).
[35]J. Hegedüs and S. R. Elliot, Nature Mat. **7**, 399 (2008).
[36]B.-S. Lee and S. G. Bishop, *Optical and Electrical Properties of Phase Change Materials in Phase Change Materials (Science and Applications)* (Springer, New York, 2009).
[37]T. S. Moss, *Optical Properties of Semiconductors* (Butterworths, London, 1959).
[38]N. F. Mott and E. A. Davis, *Electronic Processes in Non-Crystalline Materials*, 2nd ed. (Clarendon, Oxford, 1979).
[39]D. V. Tsu, J. Vac. Sci. Technol. A **17**, 1854 (1999).
[40]H.-K. Lyeo, D. G. Cahill, B.-S. Lee, J. R. Abelson, M-H. Kwon, K.-B. Kim, S. G. Bishop, and B. Cheong, Appl. Phys. Lett. **89**, 151904 (2006).
[41]R. P. Reifenberg, S. Kim, A. Gibby, Y. Zhang, M. Panzer, E. Pop, S. Wong, H.-S. Wong, and K. E. Goodson, Appl. Phys. Lett. **91**, 111904 (2007).
[42]Y. Yang, C. T. Li, S. M. Sadeghipour, H. Dieker, M. Wuttig, and M. Asheghi, J. Appl. Phys. **100**, 024102 (2006).
[43]M. Kuwahara, O. Suzuki, Y. Yamakawa, M. Taketoshi, T. Yagi, P. Fons, T. Fukaya, J. Tominaga, and T. Baba, Jpn. J. Appl. Phys. **46**, 3909 (2007).